applied sciences

MDPI

Article

A General Method to Obtain the Frequency Response Function from the Disturbance Source to the Sensitive Payload

Yihong Hou [1,2,3], Chunxue Wang [3], Peng Duan [3], Hang Yu [3], Xiangyu Zhao [1,2,3], Shanbo Chen [3] and Lei Zhang [3,*]

[1] Changchun Institute of Optics, Fine Mechanics and Physics, Chinese Academy of Sciences, Changchun 130033, China; houyihong@yeah.net (Y.H.); zhaoxiangyu2020@foxmail.com (X.Z.)
[2] University of Chinese Academy of Sciences, Beijing 100049, China
[3] Chang Guang Satellite Technology Co., Ltd., Changchun 130000, China; wangchunxue@charmingglobe.com (C.W.); duanpeng@charmingglobe.com (P.D.); yuhang@charmingglobe.com (H.Y.); ak48css@sina.com (S.C.)
* Correspondence: zhanglei@charmingglobe.com; Tel.: +86-173-9007-1964

Abstract: Microvibrations are one of the main factors contributing to platform jitter and a decline in pointing stability and precision. Among various disturbance sources, reaction wheel assembly (RWA) is one of the most significant ones and has drawn the interest of numerous scholars. How to evaluate the influence of the disturbances of RWA on the pointing accuracy of a spacecraft is an arduous task because it involves multiple disciplines. The acquisition of the frequency response function (FRF) from the disturbance source to the sensitive payload is one of the most crucial stages in integrated modeling. Direct measurement of the FRF in the six directions is challenging because of the restricted room for RWA installation in a spacecraft, particularly in small satellites. In this paper, a general method based on the $\mathbf{H}_v$ algorithm to obtain the FRF is presented. This method only needs the RWA, itself, as an excitation source. Then, in order to acquire the FRF, we use an optical remote-sensing satellite as the research object. The peak positions of FRF obtained by different RWAs are basically the same, while the amplitudes are slightly different, indicating that this method is effective. This method takes into consideration the coupling between the RWA and the spacecraft, making it possible to multiply the RWA disturbance measured at a fixed interface with the FRF, to determine the image motion of the sensitive payload.

Keywords: microvibration; integrated modeling; reaction wheel assembly; frequency response function

Citation: Hou, Y.; Wang, C.; Duan, P.; Yu, H.; Zhao, X.; Chen, S.; Zhang, L. A General Method to Obtain the Frequency Response Function from the Disturbance Source to the Sensitive Payload. *Appl. Sci.* **2023**, *13*, 4844. https://doi.org/10.3390/app13084844

Academic Editor: Rosario Pecora

Received: 10 March 2023
Revised: 2 April 2023
Accepted: 5 April 2023
Published: 12 April 2023

1. Introduction

The pointing performance of a spacecraft is continuously advancing due to the quick developments in space technology. For example, the Earth observation spacecraft [1]. The Seasat/Landsat-1, in the 1970s, had a pointing accuracy of 1°–0.3° and an attitude stability of 5×10^{-2}°/s–1×10^{-2}°/s. The SPOT/Landsat-2 satellites, in the 1980s, had a pointing accuracy of 0.3°–0.03° and an attitude stability of 3×10^{-3}°/s–3×10^{-5}°/s. The ADEOS satellite, in the 1990s, had a pointing accuracy of 0.3°–0.02° and an attitude stability of 1×10^{-3}°/s–1×10^{-6}°/s. The pointing accuracy of the Hilios/IRS-P satellites in the new century was 0.1–0.001°, and the attitude stability was better than 1×10^{-4}°/s. The same trend holds true for space telescopes and interferometers [2]. The Infrared Astronomical Satellite (IRAS) had an absolute pointing accuracy of 30 arcseconds with a pointing stability of 10 arcseconds. The Hubble Space Telescope launched on 24 April 1990, had a radial pointing stability of 0.007 arcseconds RMS over periods between 60 s and 24 h. The Infrared Space Observatory (ISO), launched on 17 November 1995, was required to achieve 11.7 arcseconds radial absolute accuracy at 2-sigma, 2.7 arcseconds half-cone stability at 2-sigma over a time period of 30 s and 2.8 arcseconds half-cone drift at 2-sigma per hour. The James Webb Space Telescope (JWST), launched on 25 December 2021, had a line-of-sight (LOS) stability that was better than 0.005 arcseconds RMS, a change in mean

pointing over a timescale of a few seconds less than 0.0035 arcseconds, and a roll stability below 0.0035 arcseconds.

To satisfy such strict requirements, a wide range of perturbation causes must be carefully taken into account. Eyerman [3] provided a thorough overview of the different disturbance sources, including both internal and external disturbance sources, which caused spacecraft' platforms to vibrate in 1990. The external disturbance sources mainly come from the spacecraft's external space environment and include torques produced from gravity gradients, atmospheric drag, radiation pressure, magnetic dipoles, particle impacts, and eclipse transients. The external disturbance sources mainly induce the low-frequency vibration of the large flexible accessory of the spacecraft platform (<1 Hz). This kind of vibration can generally be eliminated by compensation of attitude and orbit control systems (AOCS) [4] or structural vibration control of flexible attachments [5,6]. Internal disturbance sources mainly come from various moving parts inside the spacecraft, such as reaction wheel assembly (RWA), control moment gyros (CMGs), cryocoolers, solar wing driving mechanisms, antenna driving mechanisms, etc. [7]. These moving components and systems typically have non-ideal characteristics, such as residual unbalance in the rotor of the RWA, unstable output in the solar wing drive motor, etc., which cause additional disturbance while in operation. This trait is intrinsic to the moving parts on the spacecraft because these disturbance factors are essentially unavoidable. The vibration caused by the moving parts inside the spacecraft is specifically referred to as microvibrations. Although the onboard microvibration has a very small amplitude, it is one of the major factors contributing to platform jitter and a decline in pointing stability and precision. The frequency range of a microvibration is very wide (1 Hz–1000 Hz), among which the most prominent disturbance is in the range of 10–200 Hz. It goes far beyond AOCS's range. To prevent its impact on the spacecraft, it is essential to research and implement practical countermeasures.

One of the most significant sources of disturbance, RWA has drawn the attention of many academics. Examples include the empirical and analytical models of RWA disturbances, in references [8–10], parameter estimation, identification of RWA, in references [11,12], and nonlinear electromechanical coupling dynamics of RWA, in reference [13]. Evaluating the influence of the disturbance on the pointing accuracy of a spacecraft is an arduous task because it involves multiple disciplines, such as structural dynamics, control systems, mechanisms, and system engineering [14]. The integrated modeling is an efficient method, as demonstrated by the development of DOCS (Dynamics–Optics–Controls–Structures) by SSL (Space System Laboratory, Cambridge, MA, USA) at MIT [15,16], IMOS (Integrated Modeling of Optical Systems) by Jet Propulsion Laboratory (JPL) (Pasadena, CA, USA) [17], Integrated Modeling Environment (IME) by Goddard Space Flight Center (Greenbelt, MD, USA), Constellation Software Engineering (CSE) (Annapolis, MD, USA) [18], and Integrated Framework by Korea Advanced Institute of Science and Technology (Daejeon, Republic of Korea) [19].

Acquisition of the frequency response function (FRF) from the disturbance source to the sensitive payload is one of the most crucial stages in integrated modeling, and many scholars have worked hard on this [20–22]. It is challenging to measure the FRF directly due to the restricted room for RWA installation in real spacecraft, particularly in small satellites. The standard procedure is to use a shaker to measure the FRF from the location of the RWA installation to the sensitive payload. The response of the sensitive payload derived by multiplying the FRF and the disturbance force and tongue measured in a hard-mounted boundary condition is quite different from the test result because of the coupling between the RWA and the support structure. Therefore, additional complex tests are needed to compensate for the disturbance force of the RWA, such as the static dynamic mass measurement techniques, for when the RWA is at 0 rpm [23,24], the dynamic mass measurement method, which includes the gyroscopic effects in its accelerants [25,26], a combination of the experiments in a static condition, and analysis that includes the gyroscopic effect through the RWA finite element (FE) model [27].

There are many various FRF estimation techniques [28–30], yet the most widely used ones are the $\mathbf{H}_1$, $\mathbf{H}_2$, and $\mathbf{H}_v$ algorithms. The $\mathbf{H}_1$ method assumes that there is no error in the references, while the $\mathbf{H}_2$ method assumes that there is no error in the responses. The $\mathbf{H}_v$ method provides the most precise estimate by accounting for the input and output noises. This paper presents a general approach based on the $\mathbf{H}_v$ algorithm to acquire the FRF from the disturbance source to the sensitive payload, which is excited by the RWA, itself, and does not need any additional excitation source. The FRF obtained by this method accounts for the coupling between the RWA and the spacecraft, so the response of the sensitive load can be obtained by multiplying the RWA disturbance measured at a fixed interface using the FRF.

The paper is organized as follows: in Section 2, an integrated model of a high-precision optical remote sensing satellite is developed that consists of the disturbance model, structural dynamic model, and the optical model. In Section 3, a general method to obtain the FRF from the disturbance source to the sensitive payload is proposed. In Section 4, we evaluate the microvibration of the entire satellite using different RWAs as the excitation source. Finally, conclusions are drawn in Section 5.

2. Integrated Modeling

Considering a pointing scene, the pointing error is described as the difference between the actual orientation and the desired orientation of the spacecraft's LOS with respect to the target plane [31], as shown in Figure 1. It is described by two translations (e_x, e_y) and one rotation (ψ) on the target plane or by three rotations (θ, ϕ, ψ) about the body axes of the pointing system.

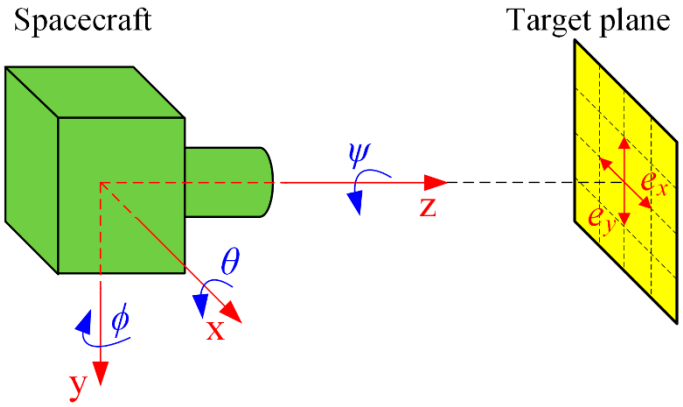

Figure 1. Schematic diagram of pointing error.

The disturbance force and torque of the RWA can result in the image motion of the sensitive optical payload. The image motion is decomposed into a sum of displacement, smear, and jitter [32,33]. The image motion $\boldsymbol{p}(t)$ can be modeled by:

$$\boldsymbol{p}(t) = \begin{bmatrix} x(t) \\ y(t) \end{bmatrix}. \tag{1}$$

In this paper, we take an optical remote-sensing satellite as the research object. The payload of the satellite is a high-resolution optical remote sensing camera with a resolution greater than 1.1 m. The satellite is in a 535 km sun-synchronous orbit and weighs 65 kg. Three RWAs were used by the satellite to change its attitude. Figure 2 depicts a 3D model of the satellite, and Table 1 lists its parameters.

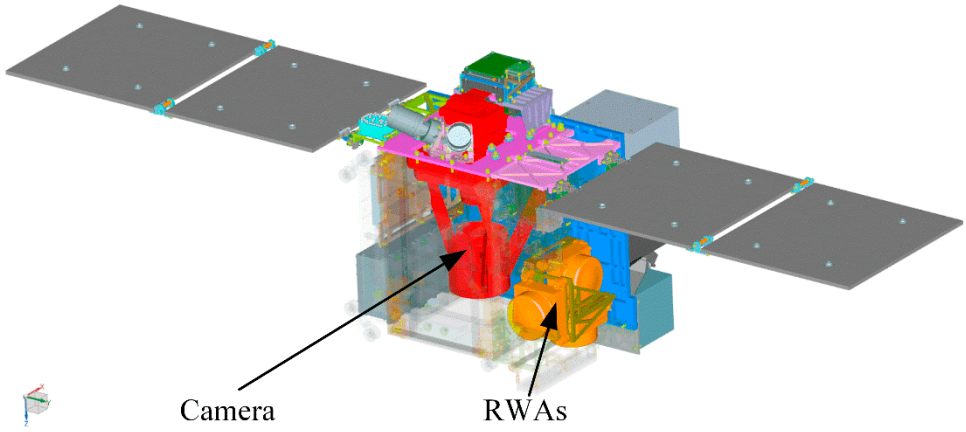

Figure 2. 3D model of the satellite.

Table 1. The parameters of the satellite.

Parameter	Value
Mass	65 kg
Orbit	535 km@SSO
Image resolution	≤1.1 m
Pointing accuracy	≤0.05° (3σ)
Attitude stability	≤0.0005°/s (3σ)
Swath width	>18.5 km
Focal length	1600 mm ± 30 mm
Image element size	3.2 μm
Static MTF	≥0.13 (Nyquist frequency)
Dynamic MTF	≥0.10 (Nyquist frequency)

The integrated model of the satellite consists of three parts, ignoring the effect of AOCS: disturbance model, structural dynamic model, and optical model. The three parts are connected to each other through input and output interfaces. The output of the disturbance model is $\boldsymbol{F}$, which acts on the structural dynamic model of the satellite and causes the camera's optics to shift slightly. This displacement $\boldsymbol{\eta}$ is used as the input of the optical model to obtain the final image motion $\boldsymbol{p}$. The block diagram of the integrated model is shown in Figure 3.

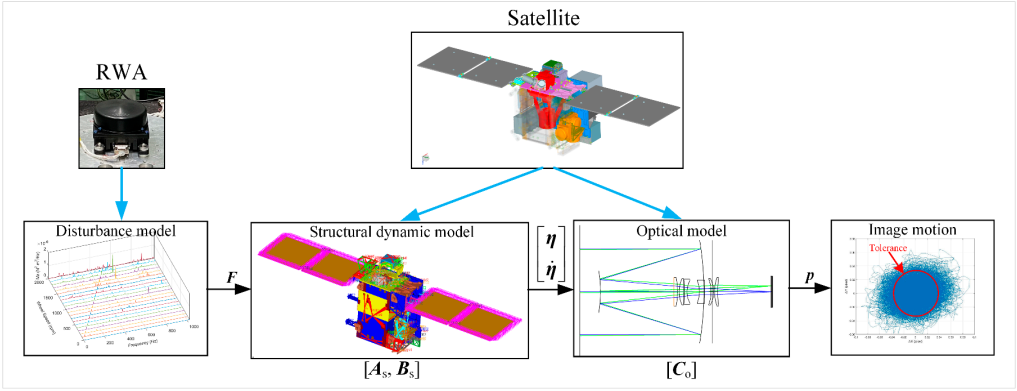

Figure 3. Block diagram of the integrated model.

2.1. Disturbance Model

RWA is the primary disturbance source in most spacecrafts and the disturbance model of the RWA has been studied for several decades. There are currently three different types of disruption disturbance models. They are the empirical model [34], the analytic model [8,9], and

the semi-analytic model [35]. This paper does not place a strong focus on the disturbance model, and in order to derive the integrated model, we use the empirical model.

The disturbance of the RWA is modeled as a series of discrete harmonics with amplitudes proportional to the square of the wheel speed and frequencies that change linearly with wheel speed [9]:

$$F_j(t) = \sum_{i=1}^{n} C_i \Omega^2 \sin(2\pi h_i \Omega t + \alpha_i) \ (j = 1, 2, \cdots, 6), \tag{2}$$

where, $F_j(t)$ is the jth component of $\boldsymbol{F}$, $\boldsymbol{F} = [F_x, F_y, F_z, M_x, M_y, M_z]^T$. n is the number of harmonics included in the model, C_i is the amplitude coefficient of the ith harmonic, Ω is the wheel speed, $h_i = \omega_i/\Omega$ is the ith harmonic number, equal to the ratio of the frequency ω_i to the wheel speed Ω, and α_i is a random phase (assumed to be uniform over $(0, 2\pi)$).

The disturbance force and tongue of RWA in the hard-mounted boundary condition can be obtained using a Kistler table, as shown in Figure 4, while the results are shown in Figure 5. It can be seen that the main harmonic numbers of F_x, F_y, M_x, and M_y are 1, 14.19, and 15.43, respectively, while the main harmonic numbers of F_z are 14.86 and 18.62 and M_z are 15.96 and 47.86.

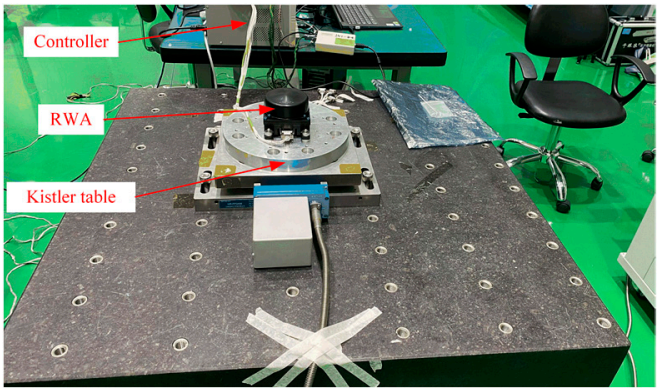

Figure 4. Test site for the RWA disturbance.

2.2. Structural Dynamic Model

The general equation that governs the structural dynamics of the satellite can be written as:

$$\boldsymbol{M\ddot{q}+C\dot{q}+Kq=F}, \tag{3}$$

where $\boldsymbol{M}$ is the mass matrix, $\boldsymbol{C}$ is the damping matrix, $\boldsymbol{K}$ is the stiff matrix, $\boldsymbol{F}$ is the disturbance force or torque, and $\boldsymbol{q}$ is the displacement response. Use the mode shape matrix to convert the physical coordinates to modal coordinates as follows:

$$\boldsymbol{q} = \boldsymbol{\Phi\eta}, \tag{4}$$

where $\boldsymbol{\Phi}$ is the mode shape matrix and $\boldsymbol{\eta}$ is the modal coordinates.

Substituting Equation (4) and the second time derivative of Equation (4) into Equation (3), equates to:

$$\boldsymbol{M\Phi\ddot{\eta}+C\Phi\dot{\eta}+K\Phi\eta=F}. \tag{5}$$

The equations forming Equation (5) are coupled. To uncouple the equations, premultiply Equation (5) by the transpose of the mode shape matrix $\boldsymbol{\Phi}^T$.

$$\boldsymbol{\Phi}^T\boldsymbol{M\Phi\ddot{\eta}+\Phi}^T\boldsymbol{C\Phi\dot{\eta}+\Phi}^T\boldsymbol{K\Phi\eta=\Phi}^T\boldsymbol{F}. \tag{6}$$

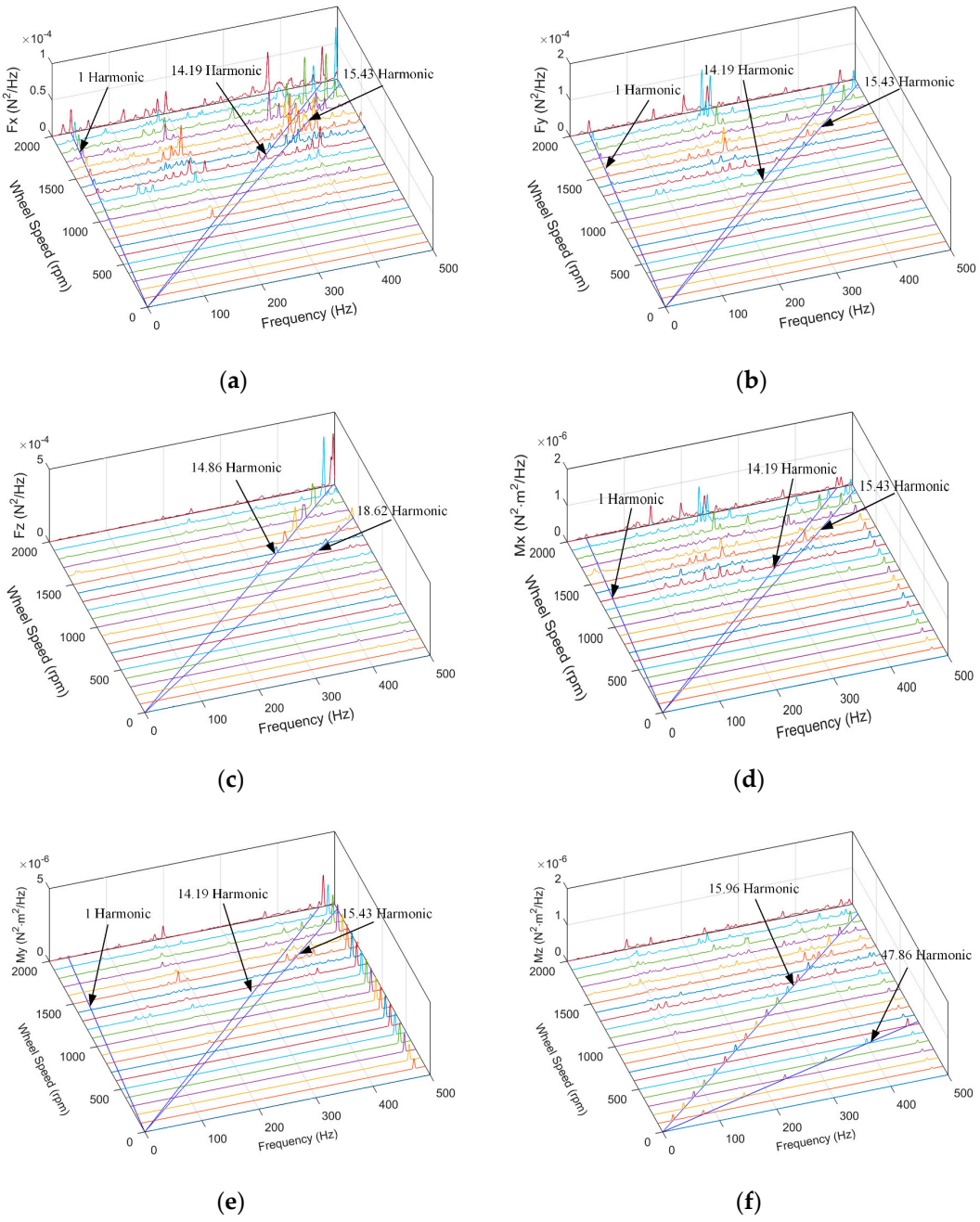

Figure 5. The disturbance force and tongue of RWA. (**a**) F_x; (**b**) F_y; (**c**) F_z; (**d**) M_x; (**e**) M_y; (**f**) M_z.

By doing so, the mass, stiffness, and damping matrices are diagonalized. The modal (generalized) mass matrix and the modal (generalized) stiffness matrix are simplified to:

$$\bar{\boldsymbol{M}} = \begin{bmatrix} 1 & & \\ & \ddots & \\ & & 1 \end{bmatrix}, \tag{7}$$

$$\bar{\boldsymbol{K}} = \begin{bmatrix} \omega_1^2 & & \\ & \ddots & \\ & & \omega_n^2 \end{bmatrix}. \tag{8}$$

While the uncoupled form of the dynamic equations can be written as:

$$\ddot{\boldsymbol{\eta}}+2\boldsymbol{\zeta\Omega}\dot{\boldsymbol{\eta}}+\boldsymbol{\Omega}^2\boldsymbol{\eta}=\boldsymbol{\Phi}^{\mathrm{T}}\boldsymbol{F}, \tag{9}$$

where the modal damping matrix is provided as:

$$\boldsymbol{\zeta} = \begin{bmatrix} \zeta_1 & & & & \\ & \ddots & & & \\ & & \zeta_i & & \\ & & & \ddots & \\ & & & & \zeta_n \end{bmatrix}. \tag{10}$$

Generally, the modal damping coefficients are different for every mode and typically vary between 0.1% and 3% for lightly damped space structures [16].

The normal frequency matrix is denoted as:

$$\boldsymbol{\Omega}^2 = \begin{bmatrix} \omega_1^2 & & \\ & \ddots & \\ & & \omega_n^2 \end{bmatrix}. \tag{11}$$

Conversion of Equation (9) to the state space form is as follows:

$$\begin{bmatrix} \dot{\boldsymbol{\eta}} \\ \ddot{\boldsymbol{\eta}} \end{bmatrix} = \begin{bmatrix} \boldsymbol{0} & \boldsymbol{I} \\ -\boldsymbol{\Omega}^2 & -2\boldsymbol{\zeta\Omega} \end{bmatrix} \begin{bmatrix} \boldsymbol{\eta} \\ \dot{\boldsymbol{\eta}} \end{bmatrix} + \begin{bmatrix} \boldsymbol{0} \\ \boldsymbol{\Phi}^{\mathrm{T}} \end{bmatrix} \boldsymbol{F} = \boldsymbol{A}_{\mathrm{s}} \begin{bmatrix} \boldsymbol{\eta} \\ \dot{\boldsymbol{\eta}} \end{bmatrix} + \boldsymbol{B}_{\mathrm{s}}\boldsymbol{F}. \tag{12}$$

2.3. Optical Model

The payload of the satellite is an optical camera of Cassegrain type. The optical system is shown in Figure 6. It is made up of a primary mirror (PM), a secondary mirror (SM), a calibration mirror (CM), and an image plane (IP).

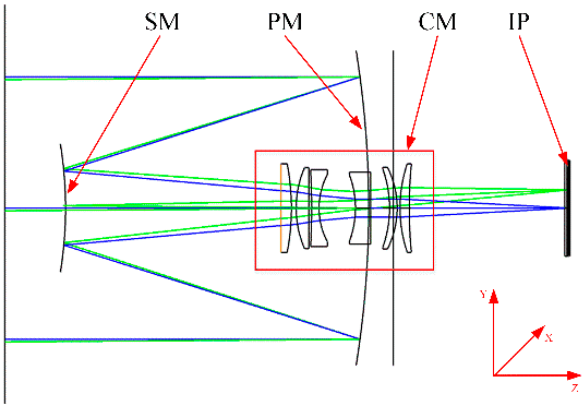

Figure 6. The optical system of the satellite.

The disturbance force and tongue will deform the optical component, which are usually small because it is very small. The deformation of each optical components can be considered a rigid-body motion. The best-fit rigid-body motion of the *i*th optical element is defined as a vector $\boldsymbol{T}_i$ of 6 terms as:

$$\boldsymbol{T}_i = \begin{bmatrix} T_{ix} & T_{iy} & T_{iz} & R_{ix} & R_{iy} & R_{iz} \end{bmatrix}^{\mathrm{T}}, \tag{13}$$

where T_{ix}, T_{iy}, and T_{iz} are translations along coordinate axes and R_{ix}, R_{iy}, and R_{iz} are rotations about coordinate axes. Then, the displacement of the node j due to these motions is [36]

$$\begin{cases} u_{ij} = T_{ix} + z_{ij}R_{iy} - y_{ij}R_{iz} \\ v_{ij} = T_{iy} - z_{ij}R_{ix} + x_{ij}R_{iz} \\ w_{ij} = T_{iz} + y_{ij}R_{ix} - x_{ij}R_{iy}, \end{cases} \tag{14}$$

where x_{ij}, y_{ij}, and z_{ij} are the coordinates of the node j, and u_{ij}, v_{ij}, and w_{ij} are the displacements of the node j. When there are n nodes on each optical component, Equation (14) is expressed as follows:

$$\boldsymbol{A}_i\boldsymbol{T}_i = \boldsymbol{q}_i, \tag{15}$$

where $\boldsymbol{q}_i = [u_{i1}, v_{i1}, w_{i1}, \cdots, u_{ij}, v_{ij}, w_{ij}, \cdots, u_{in}, v_{in}, w_{in}]^{\mathrm{T}}$, and matrix $\boldsymbol{A}_i$ is expressed as follows:

$$\boldsymbol{A}_i = \begin{bmatrix} 1 & 0 & 0 & 0 & z_{i1} & -y_{i1} \\ 0 & 1 & 0 & -z_{i1} & 0 & x_{i1} \\ 0 & 0 & 1 & y_{i1} & -x_{i1} & 0 \\ \vdots & \vdots & \vdots & \vdots & \vdots & \vdots \\ 1 & 0 & 0 & 0 & z_{ij} & -y_{ij} \\ 0 & 1 & 0 & -z_{ij} & 0 & x_{ij} \\ 0 & 0 & 1 & y_{ij} & -x_{ij} & 0 \\ \vdots & \vdots & \vdots & \vdots & \vdots & \vdots \\ 1 & 0 & 0 & 0 & z_{in} & -y_{in} \\ 0 & 1 & 0 & -z_{in} & 0 & x_{in} \\ 0 & 0 & 1 & y_{in} & -x_{in} & 0 \end{bmatrix}. \tag{16}$$

The vector $\boldsymbol{T}_i$ can be obtained from Equation (15) as follows:

$$\boldsymbol{T}_i = \boldsymbol{C}_i\boldsymbol{q}_i, \tag{17}$$

where $\boldsymbol{C}_i = (\boldsymbol{A}_i{}^{\mathrm{T}}\boldsymbol{A}_i)^{-1}\boldsymbol{A}_i{}^{\mathrm{T}}$. The matrix $\boldsymbol{C}_i$ and $\boldsymbol{q}_i$ are functions of the coordinates and displacements of node i, respectively. In order to ensure the accuracy of the fitting, n is usually greater than or equal to 3.

The image motion $\boldsymbol{p}(t)$ can be obtained by summing the product of the rigid-body motions $\boldsymbol{T}_i$ and the optical sensitivity coefficients $\boldsymbol{L}_i$ of the ith optical element.

$$\boldsymbol{p}(t) = \sum_{i=1}^{m} \boldsymbol{L}_i{}^{\mathrm{T}}\boldsymbol{T}_i, \tag{18}$$

where m is the number of optical components. $\boldsymbol{L}_i$ is defined as follows:

$$\boldsymbol{L}_i = \begin{bmatrix} \boldsymbol{L}_{ix}^{\mathrm{T}} \\ \boldsymbol{L}_{iy}^{\mathrm{T}} \end{bmatrix}^{\mathrm{T}} = \begin{bmatrix} l_{11} & l_{12} & l_{13} & l_{14} & l_{15} & l_{16} \\ l_{21} & l_{22} & l_{23} & l_{24} & l_{25} & l_{26} \end{bmatrix}^{\mathrm{T}}, \tag{19}$$

where l_{11}, l_{12}, and l_{13} represent the image motions in the x direction by translating the ith optical component one unit displacement along the x, y, and z axes, respectively. Further, l_{14}, l_{15}, and l_{16} represent the image motions in the x direction by rotating the ith optical component one unit angle about the x, y, and z axes, respectively. Moreover, l_{21}, l_{22}, and l_{23} represent the image motions in the y direction by translating the ith optical component one unit displacement along the x, y, and z axes, respectively. Finally, l_{24}, l_{25}, and l_{26} represent the image motions in the y direction by rotating the ith optical component one unit angle about the x, y, and z axes, respectively. The optical sensitivity coefficients of PM and SM, obtained by using the optical tracing method are shown in Table 2, ignoring the CM and IP.

Table 2. The optical sensitivity coefficients.

Parameter	Value	
	PM	**SM**
l_{11}	5.46	−3.79
l_{12}	0	0
l_{13}	0	0
l_{14}	0	0
l_{15}	−54.46	15.34
l_{16}	0	0
l_{21}	0	0
l_{22}	5.46	−3.79
l_{23}	0	0
l_{24}	54.46	−15.34
l_{25}	0	0
l_{26}	0	0

Substitute Equation (17) into Equation (18) and obtain:

$$\boldsymbol{p}(t) = \boldsymbol{C}_{\mathrm{o}}\boldsymbol{q}_{\mathrm{o}}, \tag{20}$$

where $\boldsymbol{q}_{\mathrm{o}} = [\boldsymbol{q}_1, \ldots, \boldsymbol{q}_2, \ldots \boldsymbol{q}_{\mathrm{m}}]^{\mathrm{T}}$. Matrix $\boldsymbol{C}_{\mathrm{o}}$ is expressed as follows:

$$\boldsymbol{C}_{\mathrm{o}} = \begin{bmatrix} \boldsymbol{L}^{\mathrm{T}}{}_{1x}\boldsymbol{C}_1 & \cdots & \boldsymbol{L}^{\mathrm{T}}{}_{ix}\boldsymbol{C}_i & \cdots & \boldsymbol{L}^{\mathrm{T}}{}_{mx}\boldsymbol{C}_m \\ \boldsymbol{L}^{\mathrm{T}}{}_{1y}\boldsymbol{C}_1 & \cdots & \boldsymbol{L}^{\mathrm{T}}{}_{iy}\boldsymbol{C}_i & \cdots & \boldsymbol{L}^{\mathrm{T}}{}_{my}\boldsymbol{C}_m \end{bmatrix}. \tag{21}$$

2.4. The Integrated Model

Divide the degrees of freedom of the satellite into the degrees of freedom of the optical component $\boldsymbol{q}_{\mathrm{o}}$ and the rest as $\boldsymbol{q}_{\mathrm{r}}$, as follows:

$$\boldsymbol{q} = \begin{bmatrix} \boldsymbol{q}_{\mathrm{o}} \\ \boldsymbol{q}_{\mathrm{r}} \end{bmatrix} = \begin{bmatrix} \boldsymbol{\Phi}_1 & \boldsymbol{\Phi}_2 & \cdots & \boldsymbol{\Phi}_k \end{bmatrix} \begin{bmatrix} \boldsymbol{\eta}_1 \\ \boldsymbol{\eta}_2 \\ \vdots \\ \boldsymbol{\eta}_k \end{bmatrix} = \begin{bmatrix} \boldsymbol{\Phi}_{\mathrm{o}1} & \boldsymbol{\Phi}_{\mathrm{o}2} & \cdots & \boldsymbol{\Phi}_{\mathrm{o}k} \\ \boldsymbol{\Phi}_{\mathrm{r}1} & \boldsymbol{\Phi}_{\mathrm{r}2} & \cdots & \boldsymbol{\Phi}_{\mathrm{r}k} \end{bmatrix} \begin{bmatrix} \boldsymbol{\eta}_1 \\ \boldsymbol{\eta}_2 \\ \vdots \\ \boldsymbol{\eta}_k \end{bmatrix}, \tag{22}$$

where k is the number of modes.

Equation (23) can be obtained from Equation (22), as follows:

$$\boldsymbol{q}_{\mathrm{o}} = \begin{bmatrix} \boldsymbol{\Phi}_{\mathrm{o}1} & \boldsymbol{\Phi}_{\mathrm{o}1} & \cdots & \boldsymbol{\Phi}_{\mathrm{ok}} \end{bmatrix} \begin{bmatrix} \boldsymbol{\eta}_1 \\ \boldsymbol{\eta}_2 \\ \vdots \\ \boldsymbol{\eta}_k \end{bmatrix} = \boldsymbol{\Phi}_{\mathrm{o}}\boldsymbol{\eta}. \tag{23}$$

Substitute Equation (23) into Equation (20) and receive:

$$\boldsymbol{p}(t) = \boldsymbol{C}_{\mathrm{o}}\boldsymbol{\Phi}_{\mathrm{o}}\boldsymbol{\eta} = \begin{bmatrix} \boldsymbol{C}_{\mathrm{o}}\boldsymbol{\Phi}_{\mathrm{o}} & \boldsymbol{0} \end{bmatrix} \begin{bmatrix} \boldsymbol{\eta} \\ \dot{\boldsymbol{\eta}} \end{bmatrix} = \boldsymbol{C}_{\mathrm{p}} \begin{bmatrix} \boldsymbol{\eta} \\ \dot{\boldsymbol{\eta}} \end{bmatrix}. \tag{24}$$

Rewrite Equations (12) and (24), and the integrated model of the satellite is provided, as follows:

$$\begin{cases} \begin{bmatrix} \dot{\boldsymbol{\eta}} \\ \ddot{\boldsymbol{\eta}} \end{bmatrix} = \boldsymbol{A}_{\mathrm{s}} \begin{bmatrix} \boldsymbol{\eta} \\ \dot{\boldsymbol{\eta}} \end{bmatrix} + \boldsymbol{B}_{\mathrm{s}}\boldsymbol{F} \\ \boldsymbol{p} = \boldsymbol{C}_{\mathrm{p}} \begin{bmatrix} \boldsymbol{\eta} \\ \dot{\boldsymbol{\eta}} \end{bmatrix}. \end{cases} \tag{25}$$

3. FRF Estimation

Applying the Laplace transform of Equation (25), we acquire the transfer function $\boldsymbol{H}(s)$ from the disturbance to the image motion, as follows:

$$\begin{cases} \boldsymbol{P}(s) = \boldsymbol{H}(s)\boldsymbol{F}(s) \\ \boldsymbol{H}(s) = \boldsymbol{C}_{\mathrm{p}}(s\boldsymbol{I} - \boldsymbol{A}_{\mathrm{s}})^{-1}\boldsymbol{B}_{\mathrm{s}}, \end{cases} \tag{26}$$

where $\boldsymbol{P}(s)$ and $\boldsymbol{F}(s)$ are the Laplace transform of $\boldsymbol{p}(t)$ and $\boldsymbol{F}(t)$, respectively.

Let $s = \mathrm{j}\omega$, then, we obtain the FRF $\boldsymbol{H}(\omega)$. The relationship between the disturbance $\boldsymbol{F}(\omega)$ and the image motion $\boldsymbol{P}(\omega)$ in the frequency domain is:

$$\boldsymbol{P}(\omega) = \boldsymbol{H}(\omega)\boldsymbol{F}(\omega), \tag{27}$$

where $\boldsymbol{F}(\omega) = [F_{\mathrm{x}}(\omega), F_{\mathrm{y}}(\omega), F_{\mathrm{z}}(\omega), M_{\mathrm{x}}(\omega), M_{\mathrm{y}}(\omega), M_{\mathrm{z}}(\omega)]^{\mathrm{T}}$, and $\boldsymbol{H}(\omega)$ is a 2×6 matrix.

In fact, when an RWA is installed on a flexible supporting structure, its disturbances excite the modes of the structure, which, in turn, perturb the RWA, itself, thus, creating coupled dynamics [24]. As a result, the loads that are present at the interface vary from those that would be found in a hard-mounted boundary condition [25–27]. The forces and moments $\boldsymbol{f}_C$ that are actually transmitted at the interface between the source and the supporting structure can be described as:

$$\boldsymbol{f}_{\mathrm{C}} = \boldsymbol{f}_{\mathrm{B}} - \boldsymbol{D}_{\mathrm{wa}}\ddot{\boldsymbol{x}}_{\mathrm{C}}, \tag{28}$$

where $\boldsymbol{f}_{\mathrm{B}}$ is the forces and moments measured in the hard-mounted boundary condition, $\boldsymbol{D}_{\mathrm{wa}}$ is the dynamic characteristics (inertia, stiffness, and damping) of the source and $\ddot{\boldsymbol{x}}_{\mathrm{C}}$ is the vector of the coupled acceleration at the interface. The acceleration vector $\ddot{\boldsymbol{x}}_{\mathrm{C}}$ can be determined if the supporting structure response at the interface node point (i.e., the dynamic mass of the supporting structure $\boldsymbol{D}_{\mathrm{ss}}$) is provided:

$$\ddot{\boldsymbol{x}}_{\mathrm{C}} = \boldsymbol{D}_{\mathrm{ss}}^{-1}\boldsymbol{f}_{\mathrm{C}}. \tag{29}$$

Substituting Equation (29) into Equation (28), Equation (28) can be rewritten as:

$$\boldsymbol{f}_{\mathrm{C}} = \boldsymbol{f}_{\mathrm{B}} - \boldsymbol{D}_{\mathrm{wa}}\boldsymbol{D}_{\mathrm{ss}}^{-1}\boldsymbol{f}_{\mathrm{C}}. \tag{30}$$

Rearrange Equation (30) and obtain $\boldsymbol{f}_C$ as:

$$\boldsymbol{f}_{\mathrm{C}} = \left(\boldsymbol{I} + \boldsymbol{D}_{\mathrm{wa}}\boldsymbol{D}_{\mathrm{ss}}^{-1}\right)^{-1}\boldsymbol{f}_{\mathrm{B}}, \tag{31}$$

where $\boldsymbol{I}$ is a 6×6-unit matrix. Equation (31) can also be reformulated in terms of the Power Spectral Density (PSD) as:

$$\boldsymbol{\Phi}_{\mathrm{C}} = \left(\boldsymbol{I} - \boldsymbol{D}_{\mathrm{wa}}\boldsymbol{D}_{\mathrm{ss}}^{-1}\right)^{-1}\boldsymbol{\Phi}_{\mathrm{B}}\left(\boldsymbol{I} - \boldsymbol{D}_{\mathrm{wa}}\boldsymbol{D}_{\mathrm{ss}}^{-1}\right)^{-\mathrm{H}}, \tag{32}$$

where $\boldsymbol{f}_{\mathrm{C}}$ and $\boldsymbol{f}_{\mathrm{B}}$ become $\boldsymbol{\Phi}_{\mathrm{C}}$ and $\boldsymbol{\Phi}_{\mathrm{B}}$, respectively, and H denotes the Hermitian transpose.

The PSD output of the image motion $\boldsymbol{\Phi}_{\mathrm{out}}$ can be obtained by multiplying the $\boldsymbol{\Phi}_{\mathrm{C}}$ by the transfer function matrix, which links the interface node point to the image motion, $\boldsymbol{TF}_{\mathrm{C-out}}$, to obtain:

$$\boldsymbol{\Phi}_{\mathrm{out}} = \boldsymbol{TF}_{\mathrm{C-out}}\left(\boldsymbol{I} - \boldsymbol{D}_{\mathrm{wa}}\boldsymbol{D}_{\mathrm{ss}}^{-1}\right)^{-1}\boldsymbol{\Phi}_{\mathrm{B}}\left(\boldsymbol{I} - \boldsymbol{D}_{\mathrm{wa}}\boldsymbol{D}_{\mathrm{ss}}^{-1}\right)^{-\mathrm{H}}\boldsymbol{TF}_{\mathrm{C-out}}^{\mathrm{H}}. \tag{33}$$

Due to the complexity of $\boldsymbol{D}_{\mathrm{wa}}$ and $\boldsymbol{D}_{\mathrm{ss}}$, many challenging experiments needed to be planned, similar to reference [25]. The transfer function from $\boldsymbol{\Phi}_{\mathrm{B}}$ to $\boldsymbol{\Phi}_{\mathrm{out}}$ is defined as:

$$\boldsymbol{TF}_{\mathrm{B-out}} = \boldsymbol{TF}_{\mathrm{C-out}}\left(\boldsymbol{I} - \boldsymbol{D}_{\mathrm{wa}}\boldsymbol{D}_{\mathrm{ss}}^{-1}\right)^{-1}. \tag{34}$$

The PSD output of the image motion $\boldsymbol{\Phi}_{\text{out}}$ can be rewritten as:

$$\boldsymbol{\Phi}_{\text{out}} = \boldsymbol{TF}_{\text{B}-\text{out}} \boldsymbol{\Phi}_{\text{B}} \boldsymbol{TF}_{\text{B}-\text{out}}^{\text{H}}. \tag{35}$$

$\boldsymbol{TF}_{\text{B-out}}$ can be obtained by the $\mathbf{H}_{\text{v}}$ algorithm, by taking into account both the input and output noises [28–30]. The following is a brief introduction to the $\mathbf{H}_{\text{v}}$ algorithm. The augmented characteristic matrix $\boldsymbol{G}_{\text{FFX}}$ can be compiled as shown in Equation (34).

$$\boldsymbol{G}_{\text{FFX}} = \begin{bmatrix} \boldsymbol{G}_{\text{FF}} & \boldsymbol{G}_{\text{FX}} \\ \boldsymbol{G}_{\text{XF}} & \boldsymbol{G}_{\text{XX}} \end{bmatrix}, \tag{36}$$

where $\boldsymbol{G}_{\text{FF}}$ and $\boldsymbol{G}_{\text{XX}}$ are the auto power matrixes of the input (disturbance force and tongue of RWA) and output (image motion in X direction), respectively. $\boldsymbol{G}_{\text{FX}}$ and $\boldsymbol{G}_{\text{XF}}$ are the cross-power matrixes of input and output. The singular value decomposition of $\boldsymbol{G}_{\text{FFX}}$ results in a diagonal eigenvalue matrix $\boldsymbol{\Lambda}$ and an eigenvector matrix $\boldsymbol{V}$.

$$\boldsymbol{G}_{\text{FFX}} = \boldsymbol{V}\boldsymbol{\Lambda}\boldsymbol{V}^{\text{H}}. \tag{37}$$

Choosing the column of $\boldsymbol{V}$ representing the eigenvector, corresponding to the smallest eigenvalue and normalizing it, such that its last element is -1, the $\mathbf{H}_{\text{v}}$ estimate can be obtained as shown in Equation (38):

$$V_{\lambda_{\min}} = \begin{bmatrix} H_{11} \\ H_{12} \\ \vdots \\ H_{16} \\ -1 \end{bmatrix} = \begin{bmatrix} \boldsymbol{H}_v^T \\ -1 \end{bmatrix}, \tag{38}$$

when the augmented characteristic matrix becomes $\boldsymbol{G}_{\text{FFY}}$, we can obtain [$H_{21}$, H_{22}, H_{23}, H_{24}, H_{25}, H_{26}] using the same method.

In order to reduce the estimation error of the FRF, geometrically average the FRF at different speeds, as follows:

$$\boldsymbol{H}_{ij} = \sqrt[21]{\prod_{k=1}^{k=21} \boldsymbol{H}_{ij-k}} (i = 1, 2, j = 1, 2, \cdots, 6), \tag{39}$$

where $\boldsymbol{H}_{\text{ij}-\text{k}}$ is the FRF $\boldsymbol{H}_{\text{ij}}$ at $100 \times (k-1)$ rpm.

The coherence function is often introduced to evaluate the reliability of FRF. It is defined as the measure of the causal relationship between two signals with the presence of other signals. For the ith output and the jth input, the coherence function is formulated, as in [28]

$$\gamma_{ij}^2 = \frac{|G_{\text{XF}}(i,j)|^2}{G_{\text{FF}}(j,j) G_{\text{XX}}(i,i)}. \tag{40}$$

When the coherence function is equal to one, the two signals are completely related. If the coherence function between two input signals is 0, then, the two inputs are completely unrelated.

4. Experiment and Discussion

RWA is one of the most important disturbance sources on the satellite. We used the RWA disturbance as the excitation source to acquire the FRF from the disturbance source to the sensitive payload. The test platform of microvibration was built, as shown in Figure 7, and mainly composed of the satellite, low-frequency suspension system, RWA controller, and signal acquisition system. Five acceleration sensors (numbered a1–a5) and three acceleration sensors (numbered a6–a8) were connected to the PM and the SM, respectively.

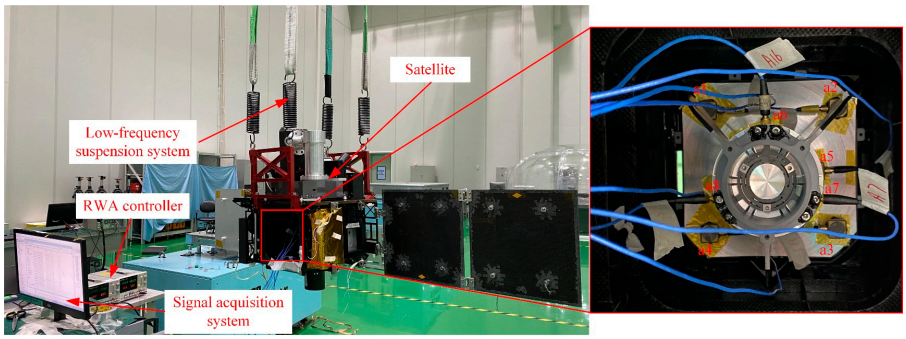

Figure 7. Test platform for the microvibration.

We collected the acceleration information of the 8 sensors, when the RWA increased from 0 to 2000 rpm, at every 100 rpm. The accelerations of a1 sensor in 3 directions at 2000 rpm are shown in Figure 8. The figure shows that the test's signal-to-noise ratio was high and satisfied the test requirements.

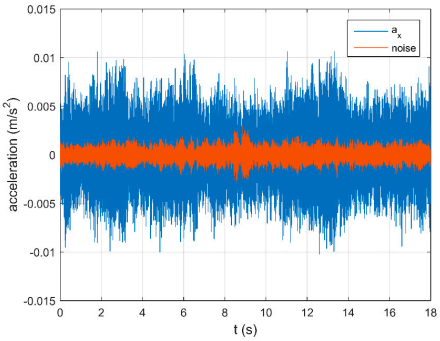

(**a**)

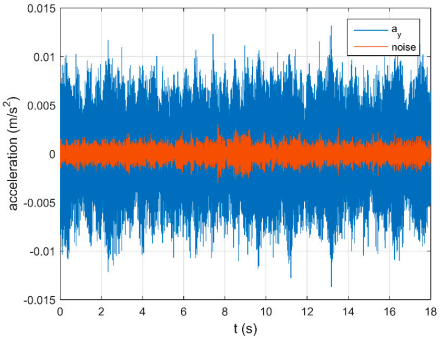

(**b**)

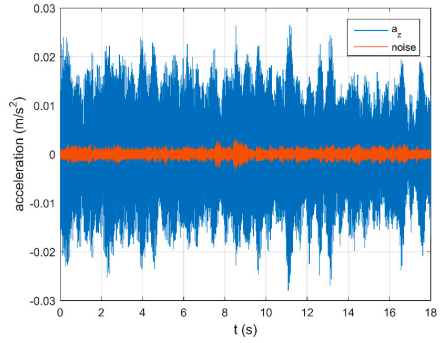

(**c**)

Figure 8. The accelerations of a1 sensor at 2000 rpm. (**a**) a_x; (**b**) a_y; (**c**) a_z.

The gathered acceleration signals were transformed into displacement signals by quadratic integration, in order to fit the rigid-body displacement of each optical element, using Equation (17). Then, the image motion at each speed can be calculated by Equation (20). Through Equation (19), it is possible to determine the image motion at each speed, including the image motion at 0 rpm, 500 rpm, 1000 rpm, and 2000 rpm, as shown in Figure 9. The waterfall of the image motion is shown in Figure 10. The picture shows that when the RWA is at 600 rpm, there is a significant amplitude at 159.8 Hz.

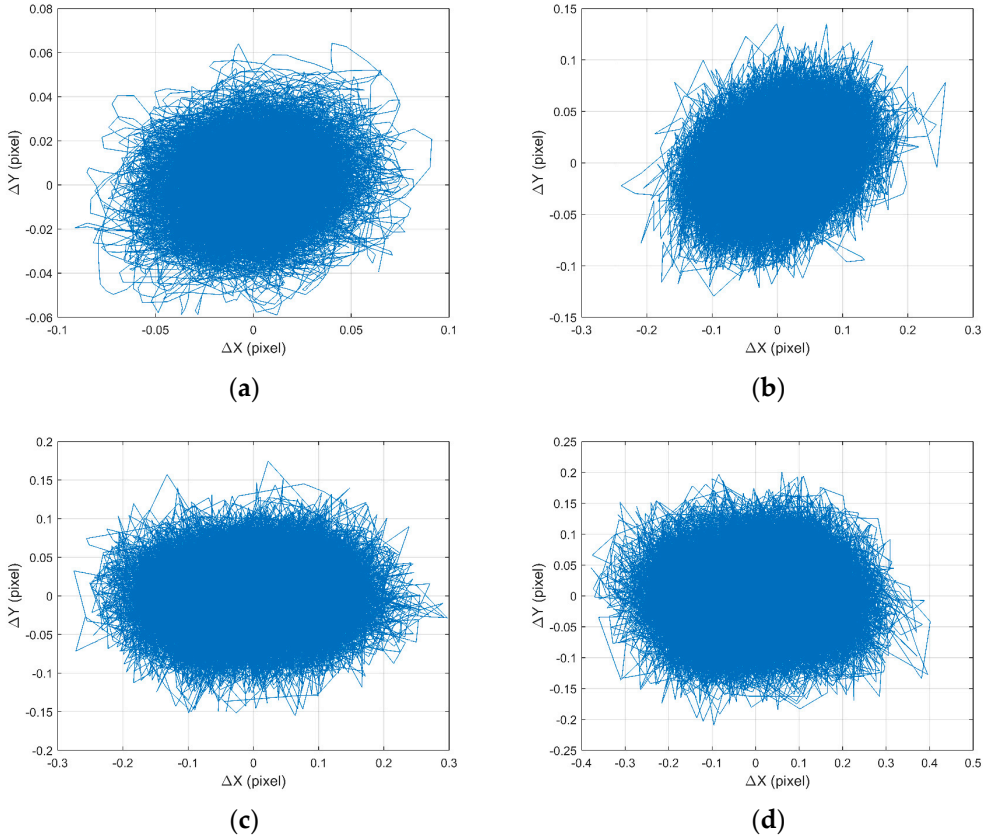

Figure 9. The image motion at each speed. (**a**) 0 rpm; (**b**) 500 rpm; (**c**) 1000 rpm; (**d**) 2000 rpm.

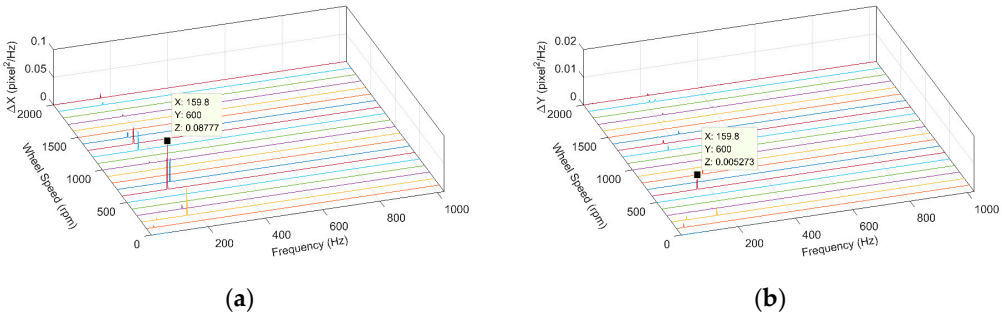

Figure 10. The waterfall of image motion. (**a**) x-direction; (**b**) y-direction.

The FRF and coherence function at 600 rpm are shown in Figure 11. For simplicity, only H_{16} and H_{26} are shown. The figure shows that the coherence at 159.5 Hz is roughly equivalent to 0.8, demonstrating the dependability of the FRF at this frequency.

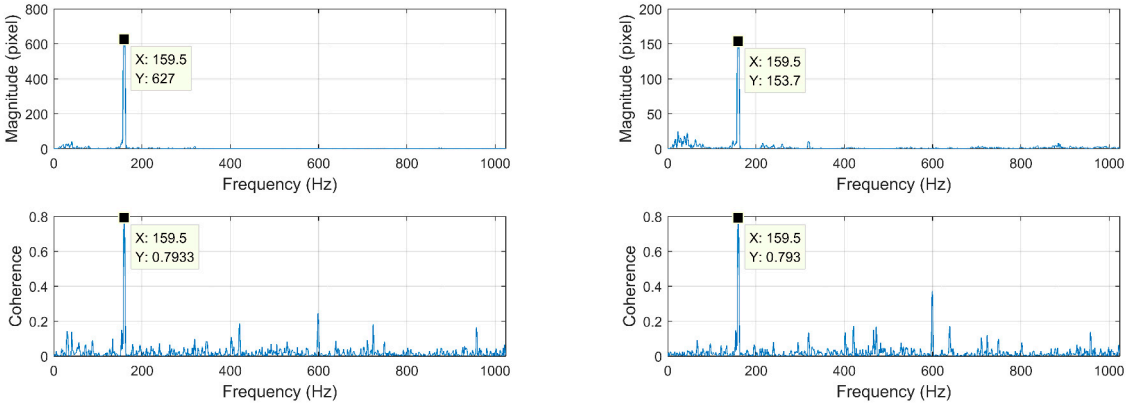

(**a**) (**b**)

Figure 11. The FRF and coherence at 600 rpm. (**a**) H_{16}; (**b**) H_{26}.

We can obtain the average value of the FRF at different speeds using Equation (39). We performed the same test using three distinct RWAs numbered Z01, Z02, and Z03, to validate the methodology suggested in this paper. The outcomes are depicted in Figure 12.

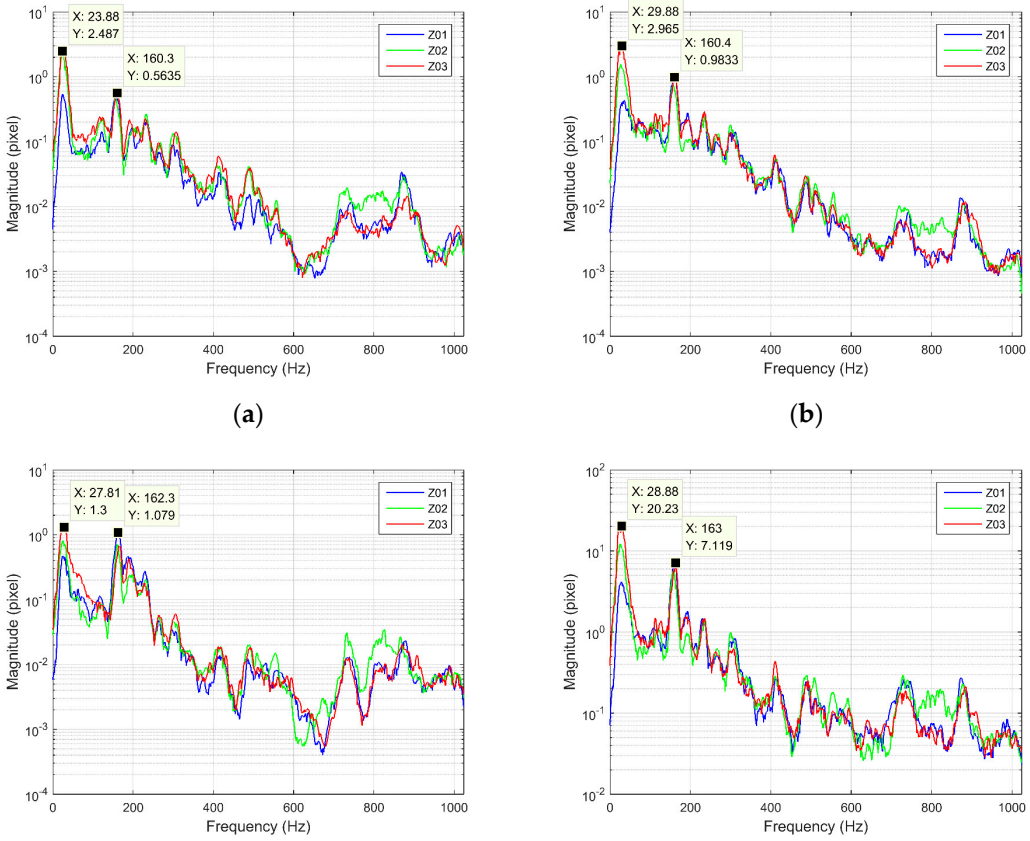

(**a**) (**b**)

(**c**) (**d**)

Figure 12. *Cont.*

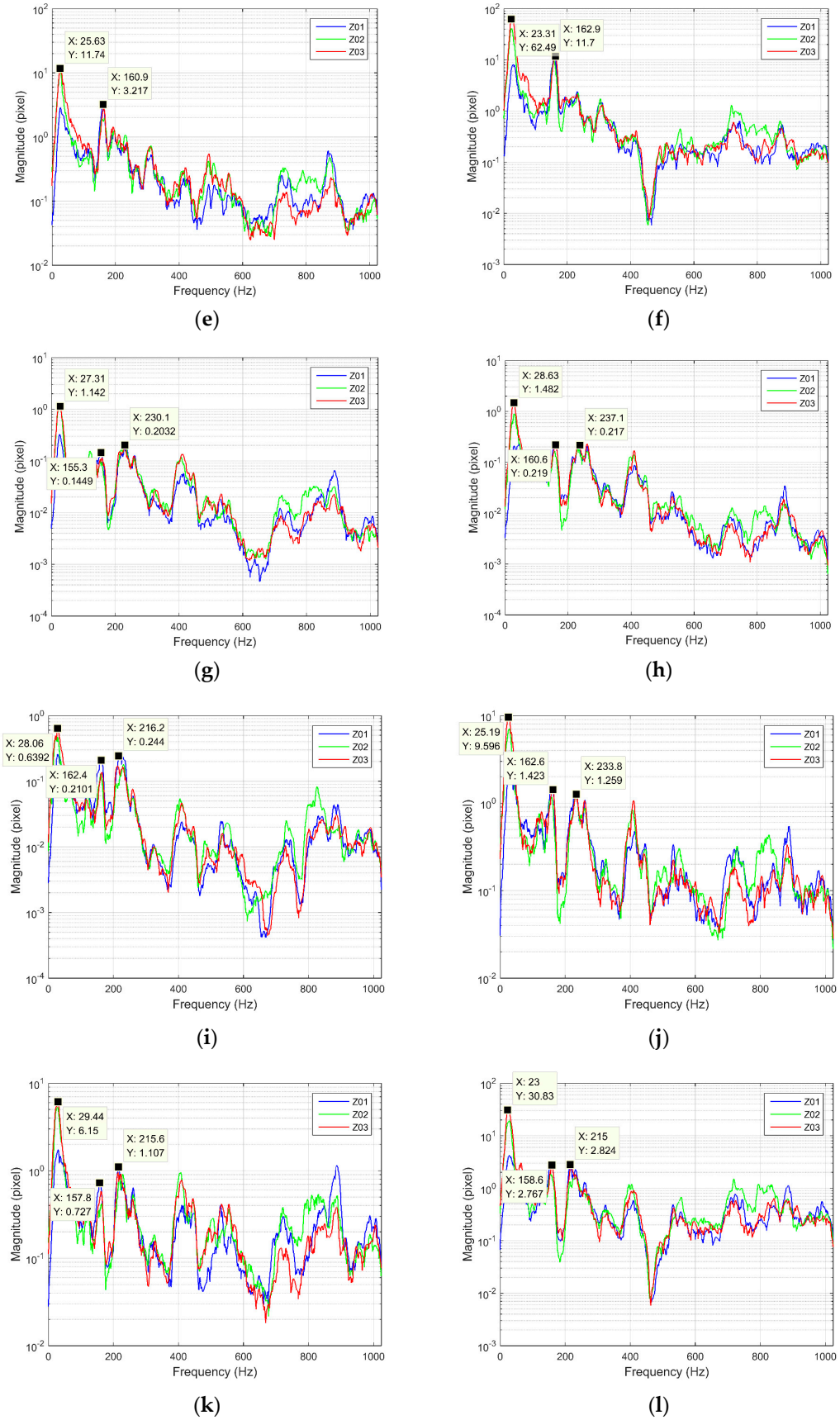

Figure 12. The FRF was obtained by different RWAs. (**a**) H_{11}; (**b**) H_{12}; (**c**) H_{13}; (**d**) H_{14}; (**e**) H_{15}; (**f**) H_{16}; (**g**) H_{21}; (**h**) H_{22}; (**i**) H_{23}; (**j**) H_{24}; (**k**) H_{25}; (**l**) H_{26}.

As can be seen from Figure 12, the amplitude of the FRF for the low frequency is larger, especially between 23 Hz–30 Hz, 155 Hz–163 Hz, and 215 Hz–237 Hz. Due to the influence of noise, the amplitude of the FRF obtained by different RWAs at 23 Hz–30 Hz differs greatly, while the differences at other frequencies are small. The figure also demonstrates that, at frequencies around 160 Hz, F_x has the least impact on the image motion in the x direction compared to F_z and F_y, while M_z has the greatest influence compared with M_x and M_y. Further, M_z, M_x, and M_y have a decreasing impact on the image motion in the y direction, near 230 Hz, while F_x, F_y, and F_z have the same effect.

5. Conclusions

In this paper, a general method that would obtain the FRF from the disturbance source to the sensitive payload was proposed. Firstly, the integrated model of a high-precision optical remote sensing satellite was developed, including the disturbance mode, structural dynamic mode, and optical mode, while the effect of AOCS was ignored. Secondly, a general method based on the $\mathbf{H}_v$ algorithm was presented to obtain the FRF, which does not require an additional excitation source, except for the RWA itself. Finally, a microvibration test of the satellite using different RWAs was carried out. The experimental results demonstrate that the coherence is high, and the peak positions of the FRF obtained by different RWAs are basically the same, while the amplitudes are slightly different, especially at 23 Hz–30 Hz, which indicates that the method proposed in this paper is effective. Therefore, the image motion of the sensitive payload can be obtained by multiplying the disturbance of the RWA measured at a fixed interface with the FRF, and without extensive testing when changing different RWAs in the same series.

Author Contributions: Conceptualization, Y.H.; data curation, Y.H., C.W., P.D. and H.Y.; formal analysis, Y.H.; funding acquisition, L.Z.; investigation, Y.H.; methodology, Y.H. and S.C.; project administration, L.Z.; resources, S.C. and L.Z.; software, Y.H. and H.Y.; validation, Y.H. and P.D.; visualization, X.Z. and L.Z.; writing—original draft, Y.H.; writing—review and editing, Y.H. and C.W. All authors have read and agreed to the published version of the manuscript.

Funding: This research was funded by the Jilin Province Science and technology development plan project of China, Grant No. 20210508038RQ.

Institutional Review Board Statement: Not applicable.

Informed Consent Statement: Not applicable.

Data Availability Statement: Not applicable.

Conflicts of Interest: The authors declare no conflict of interest.

References

1. Wang, J.; Li, D.-X. *Rigid-Flexible Coupling Dynamics and Control of Flexible Spacecraft with Time-Varying Parameters*; Springer Nature: Berlin, Germany, 2021.
2. Blackmore, L.; Murray, E.; Scharf, D.P.; Aung, M.; Bayard, D.; Brugarolas, P.; Hadaegh, F.; Lee, A.; Milman, M.; Sirlin, S. *Instrument Pointing Capabilities: Past, Present, and Future*; NASA: Washington, DC, USA, 2011.
3. Eyerman, C.E. A systems Engineering Approach to Disturbance Minimization for Spacecraft Utilizing Controlled Structures Technology. Ph.D. Thesis, Massachusetts Institute of Technology, Cambridge, MA, USA, 1990.
4. Di Gennaro, S. Adaptive robust stabilization of rigid spacecraft in presence of disturbances. In Proceedings of the 1995 34th IEEE Conference on Decision and Control, New Orleans, LA, USA, 13–15 December 1995; pp. 1147–1152.
5. Li, D.; Liu, W.; Lei, Y.; Sun, X. Dynamic model for large multi-flexible-body space structures. *Int. J. Struct. Stab. Dyn.* **2014**, *14*, 1350072. [CrossRef]
6. Jiang, J.-P.; Li, D.-X. Robust H∞ vibration control for smart solar array structure. *J. Vib. Control.* **2011**, *17*, 505–515. [CrossRef]
7. Agrawal, B. Jitter control for imaging spacecraft. In Proceedings of the 2009 4th International Conference on Recent Advances in Space Technologies, Istanbul, Turkey, 11–13 June 2009; pp. 615–620.
8. Masterson, R.A. Development and Validation of Empirical and Analytical Reaction Wheel Disturbance Models. Ph.D. Thesis, Massachusetts Institute of Technology, Cambridge, MA, USA, 1999.

9. Masterson, R.A.; Miller, D.W.; Grogan, R.L. Development and Validation of Reaction Wheel Disturbance Models: Empirical Model. *J. Sound Vib.* **2002**, *249*, 575–598. [CrossRef]
10. Addari, D. *A Semi-Empirical Approach for the Modelling and Analysis of Microvibration Sources On-Board Spacecraft*; University of Surrey: London, UK, 2016.
11. Kim, D.-K. Micro-vibration model and parameter estimation method of a reaction wheel assembly. *J. Sound Vib.* **2014**, *333*, 4214–4231. [CrossRef]
12. Yang, L.; Wang, Y.-S.; Wei, L. A novel identification method for micro-vibration analysis of reaction wheel assembly. *Acta Astronaut.* **2022**, *196*, 94–106. [CrossRef]
13. Aghalari, A.; Shahravi, M. Nonlinear electromechanical modelling and dynamical behavior analysis of a satellite reaction wheel. *Acta Astronaut.* **2017**, *141*, 143–157. [CrossRef]
14. Dennehy, C.J.; Wolf, A.A.; Swanson, D.K. *Spacecraft Line-Of-Sight Jitter Management and Mitigation Lessons Learned and Engineering Best Practices*; NASA: Washington, DC, USA, 2021.
15. De Weck, O.L. Integrated Modeling and Dynamics Simulation for the Next Generation Space Telescope. Ph.D. Thesis, Massachusetts Institute of Technology, Cambridge, MA, USA, 1999.
16. Miller, D.W.; De Weck, O.L.; Mosier, G.E. Framework for multidisciplinary integrated modeling and analysis of space telescopes. In *Integrated Modeling of Telescopes*; SPIE: Bellingham, WA, USA, 2002; pp. 1–18.
17. Briggs, H. Integrated modeling and design of advanced optical systems. In Proceedings of the Aerospace Design Conference, Irvine, CA, USA, 3–6 February 1992; p. 1249.
18. Stone, C.M.; Holtery, C. The JWST integrated modeling environment. In Proceedings of the 2004 IEEE Aerospace Conference Proceedings (IEEE Cat. No. 04TH8720), Big Sky, MT, USA, 6–13 March 2004; pp. 4041–4047.
19. Lee, D.-O.; Yoon, J.-S.; Han, J.-H. Integrated framework for jitter analysis combining disturbance, structure, vibration isolator and optical model. In Proceedings of the Active and Passive Smart Structures and Integrated Systems 2012, Denver, CO, USA, 30 April 2012; pp. 677–684.
20. Neat, G.W.; Melody, J.W.; Lurie, B.J. Vibration attenuation approach for spaceborne optical interferometers. *IEEE Trans. Control. Syst. Technol.* **1998**, *6*, 689–700. [CrossRef]
21. Dekens, F.G.; Neat, G.W. Microprecision interferometer: Pointing system performance in on-orbit disturbance environment. In Proceedings of the Smart Structures and Materials 1999: Smart Structures and Integrated Systems, Newport Beach, CA, USA, 1–4 March 1998; pp. 426–439.
22. Toyoshima, M.; Jono, T.; Takahashi, N.; Yamawaki, T.; Nakagawa, K.; Arai, K. Transfer functions of microvibrational disturbances on a satellite. In Proceedings of the 21st International Communications Satellite Systems Conference and Exhibit, Yokohama, Japan, 15–19 April 2003; p. 2406.
23. Elias, L.; Miller, D. A coupled disturbance analysis method using dynamic mass measurement techniques. In Proceedings of the 43rd AIAA/ASME/ASCE/AHS/ASC Structures, Structural Dynamics, and Materials Conference, Denver, CO, USA, 22–25 April 2002; p. 1252.
24. Elias, L.M.; Dekens, F.G.; Basdogan, I.; Sievers, L.A.; Neville, T. Methodology for modeling the mechanical interaction between a reaction wheel and a flexible structure. In *Interferometry in Space*; SPIE: Bellingham, WA, USA, 2003; pp. 541–555.
25. Zhang, Z.; Aglietti, S.G.; Ren, W. Coupled microvibration analysis of a reaction wheel assembly including gyroscopic effects in its accelerance. *J. Sound Vib.* **2013**, *332*, 5748–5765. [CrossRef]
26. Addari, D.; Aglietti, G.S.; Remedia, M. Dynamic mass of a reaction wheel including gyroscopic effects: An experimental approach. *AIAA J.* **2017**, *55*, 274–285. [CrossRef]
27. Addari, D.; Aglietti, G.S.; Remedia, M. Experimental and numerical investigation of coupled microvibration dynamics for satellite reaction wheels. *J. Sound Vib.* **2017**, *386*, 225–241. [CrossRef]
28. He, J.; Fu, Z. Multi-input multi-output modal analysis methods. In *Modal Analysis*; Butterworth-Heinemann: Oxford, UK, 2001; pp. 198–223.
29. Allemang, R.J.; Patwardhan, R.S.; Kolluri, M.M.; Phillips, A.W. Frequency response function estimation techniques and the corresponding coherence functions: A review and update. *Mech. Syst. Signal Process.* **2022**, *162*, 108100. [CrossRef]
30. Allemang, R.; Avitabile, P. *Handbook of Experimental Structural Dynamics*; Springer Nature: Berlin/Heidelberg, Germany, 2022.
31. Ott, T.; Benoit, A.; Van den Braembussche, P.; Fichter, W. Esa pointing error engineering handbook. In Proceedings of the 8th International ESA Conference on Guidance, Navigation & Control Systems, Karlovy Vary, Czech Republic, 5–10 June 2011; p. 17.
32. Pittelkau, M.; McKinley, W. Pointing Error Metrics: Displacement, Smear, Jitter, and Smitter with Application to Image Motion MTF. In Proceedings of the AIAA/AAS Astrodynamics Specialist Conference, Minneapolis, MN, USA, 13–16 August 2012.
33. Pittelkau, M.E.; McKinley, W.G. Optical transfer functions, weighting functions, and metrics for images with two-dimensional line-of-sight motion. *Opt. Eng.* **2016**, *55*, 063108. [CrossRef]
34. Hasha, M. Reaction wheel mechanical noise variations. *Space Telesc. Program Eng. Memo SSS* **1986**, *218*, 175–183.

35. Liu, K.-C.; Maghami, P.; Blaurock, C. Reaction wheel disturbance modeling, jitter analysis, and validation tests for solar dynamics observatory. In Proceedings of the AIAA Guidance, Navigation and Control Conference and Exhibit, Honolulu, HI, USA, 18–21 August 2008; p. 7232.
36. Victor, L.; Keith, B.; Gregory, J. *Optical Performance as a Function Dynamic Mechanical Loading*; SPIE: Bellingham, WA, USA, 2008; pp. 1–6.